Front. Phys. 11(4), 110308 (2016)
DOI 10.1007/s11467-016-0540-2

REVIEW ARTICLE

Non-canonical distribution and non-equilibrium transport beyond weak system-bath coupling regime: A polaron transformation approach

Dazhi Xu, Jianshu Cao†

Department of Chemistry, Massachusetts Institute of Technology, Cambridge, MA 02139, USA

Corresponding author. E-mail: †*jianshu@mit.edu*

Received October 12, 2015; accepted February 2, 2016

The concept of polaron, emerged from condense matter physics, describes the dynamical interaction of moving particle with its surrounding bosonic modes. This concept has been developed into a useful method to treat open quantum systems with a complete range of system-bath coupling strength. Especially, the polaron transformation approach shows its validity in the intermediate coupling regime, in which the Redfield equation or Fermi's golden rule will fail. In the polaron frame, the equilibrium distribution carried out by perturbative expansion presents a deviation from the canonical distribution, which is beyond the usual weak coupling assumption in thermodynamics. A polaron transformed Redfield equation (PTRE) not only reproduces the dissipative quantum dynamics but also provides an accurate and efficient way to calculate the non-equilibrium steady states. Applications of the PTRE approach to problems such as exciton diffusion, heat transport and light-harvesting energy transfer are presented.

Keywords polaron transformation, strong coupling, quantum transport, non-equilibrium steady state

PACS numbers 71.38.-k, 66.10.C-, 05.60.Gg, 05.70.Ln

Contents

1 Introduction 1
2 Polaron transformation of the spin-boson model 3
3 Equilibrium distribution of the SBM via the polaron approach 4
3.1 Accuracy of the perturbation theory in the polaron frame 4
3.2 Non-canonical equilibrium distribution 6
4 Polaron transformed Redfield equation 7
4.1 Steady states and equilibrium distribution 7
4.2 Validity of the PTRE 8
4.3 Weak and strong coupling limits 8
5 Applications of PTRE to exciton diffusion, heat transport and energy transfer 9
5.1 Coherent exciton transport in disordered systems 9
5.2 Non-equilibrium heat transfer through quantum dot 10
5.3 Energy transfer via three-level heat engine model 12
6 Summary 13
Acknowledgements 14
Appendix A Correlation functions in Eq. (18) 14
Appendix B Redfield tensor in Eqs. (42) and (43) 14
Appendix C Details in non-equilibrium energy flux of Eq. (48) 14
References 15

1 Introduction

Understanding the behavior of open quantum systems, has become increasingly important in physics and chemistry as well as in technological developments. Often, the coupling between the system and the bath is considered as a small parameter compared to the characteristic energy scale of the system. This consideration leads to many natural physical results such as the canonical

*Special Topic: Progress in Open Quantum Systems: Fundamentals and Applications.

© Higher Education Press and Springer-Verlag Berlin Heidelberg 2016

Frontiers of Physics

property of equilibrium states and the negligible back action from the system to the bath. In this case, the second-order perturbation theory leads to a master equation of the Redfield or the Lindblad type [1–4], which is convenient for analytical investigation and not computationally expensive for numerical implementation. However, in many physical systems of current interest, the system-bath coupling (SBC) is comparable to the system internal couplings, hence the weak coupling approximation is not justified. The typical examples are the excitation energy transfer process in solid quantum dots [5, 6] and photosynthetic complexes [7–10]. There are a number of non-perturbative techniques to obtain the numerically exact dynamics; examples include the hierarchy master equation [11, 12], the quasi-adiabatic propagator path integral (QUAPI) [13], the density matrix renormalization group [14], the numerical renormalization group [15], the multi-configuration time-dependent Hartree approach [16, 17] and the stochastic path integrals [18, 19]. However, these methods are computationally demanding and non-trivial to implement for large systems. In addition, much of the recent efforts focus on the short-time non-Markovian dynamics (i.e., dynamical coherence), which is relevant for laser-induced coherence but not for the long-time behavior.

Therefore, we need a method which is formally simple and physically transparent, meanwhile goes beyond weak SBC regime without loosing accuracy. Polaron, a basic concept in condense matter physics, which describes the quantum (quasi-) particle interacting with the deformed lattices through electromagnetic interaction [20, 21] (as illustrated in Fig. 1), is exploited to achieve this goal. Initiated by Silbey and coworkers, a variational polaron transformation method was applied to study the bath renormalisation effects on the tunneling matrix elements in the spin-boson model (SBM) [22, 23]. Further, this approach is used to investigate the excitation migration in molecular crystals, covering both the coherent and incoherent transport preterites [24]. Recently, a polaron transformed second-order master equation has been derived to study the dynamics of open quantum systems at strong coupling [25–28]. This approach extends the regime of validity of the master equation to stronger system-bath couplings, provided that the internal couplings (or tunneling matrix elements) are small compared to the typical bath frequency (i.e., the bath response is fast on the system time-scale). The main idea of the polaron transformation approach is to describe the system in the polaron frame such that the system is dressed by the environment. The dressed system (or polaron) takes the major effects of the system-bath interaction into consideration, hence the reduced SBC is weakened to the regime that the second-order perturbation theory is applicable.

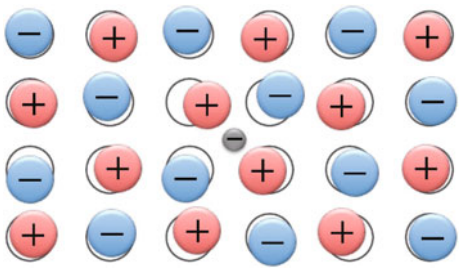

Fig. 1 Illustration of polaron formed with a charged particle surrounded by a polarized crystal medium.

In this review, we mainly focus on the polaron effects on the equilibrium and non-equilibrium steady states of multiple-level open quantum systems. The transient dynamics of an open quantum system reveals its dissipative and dephasing properties, as well as the short-time behavior in the presence of control or driving against the noise. However, many systems such as the natural photosynthetic complexes and the artificial quantum nanodevices, the open systems continuously operate at their equilibrium or non-equilibrium steady states. In these cases, we are only interested in the long-time states of the open quantum system whose properties are constant, two aspects of which will be addressed in this paper:

(i) To investigate properties of the equilibrium steady state beyond the weak SBC regime, the polaron transformation can be directly applied to the canonical density of matrix of the total system. Then a perturbative expansion with respect to the normalized SBC reveals the polaron effects on the reduced density of matrix (RDM) of the open system [29, 30], which results in the non-canonical state of the reduced system [30–32].

(ii) Another interesting issue arises when the quantum system is surrounded by the non-equilibrium environment. The characteristics of the non-equilibrium steady state are closely related with the transport quantities, such as the diffusion constant [28], the energy transfer flux [33] and the transfer efficiency [34]. The polaron transformed Redfield equation (PTRE) is suitable for these non-equilibrium problems. The SBC effectively obtained from the polaron transformation is weak enough to introduce the perturbative approach, then the resulting Redfield equation is easily manipulated to yield both the dynamics and the steady states in a broad SBC regime.

In Section 2, we present the general expression for the variational polaron transformation using the SBM as example. The full polaron transformation which is accurate for the fast bath case is straightforwardly obtained by setting the variational parameter equals to the SBC

strength. In Section 3, we obtain the equilibrium steady state by the perturbative expansion in the variational polaron frame. The comparisons with other perturbative methods and the exact numerical calculation are also presented to clarify the valid parameter regimes. The PTRE is introduced in Section 4, by which both the dynamics and the non-equilibrium steady states can be studied beyond weak coupling regime. In Section 5, three specific topics on the excitation transport and energy transfer are studied via the PTRE: the coherent quantum transport in disordered systems, non-equilibrium energy transfer via a two-level quantum dot, and non-equilibrium properties of a three-level heat engine model. We summarize the polaron approach and its application in Section 6.

2 Polaron transformation of the spin-boson model

We introduce the polaron transformation via the SBM, which is the simplest dissipative model used to investigate the energy transfer in light harvesting systems [35, 36], decoherence in atom-photon interaction systems [37], tunneling phenomena in condensed media [38, 39], charge transfer [40], and quantum phase transitions [41, 42]. The SBM describes a two-level system (TLS) coupled with a multi-mode harmonic bath. The SBM Hamiltonian is written as (we set $\hbar = 1$ in the following)

$$H_{tot} = \frac{\epsilon}{2}\sigma_z + \frac{\Delta}{2}\sigma_x + \sum_k \omega_k b_k^\dagger b_k + \sigma_z \sum_k g_k(b_k^\dagger + b_k), \tag{1}$$

where σ_i $(i = x,\ y,\ z)$ are the Pauli matrices, ϵ is the energy splitting between the two local energy levels, and Δ is the tunneling matrix element. The bath is modeled as a set of harmonic oscillators labeled by their frequencies ω_k, and their coupling strength to the TLS are denoted by g_k.

Though the SBM model is formally simple, it displays the competition between coherent (tunneling dominates) and incoherent (bath dominates) effects. Despite its simplicity, the SBM has not been solved exactly so far. Comparing with the non-trivial analytical investigation base on path integrals [38, 39] and the numerically exact but computationally demanding methods (such as the hierarchy master equation [11] and the QUAPI [13]), the polaron transformation method is clear in physical pictures, accurate in a broad range of SBC strength, and can be easily extended to multilevel systems.

For generality, the variational approach of polaron transformation is adopted here, which extends the validity of the original full polaron method to the slow bath regime [22, 23, 43]. The variational polaron transformation is generated by

$$U = \exp(-\mathrm{i}\sigma_z B/2) \tag{2}$$

with the bath operator $B = 2\mathrm{i}\sum_k \frac{f_k}{\omega_k}(b_k^\dagger - b_k)$, which displaces the bath oscillators in the positive or negative direction depending on the state of the TLS. The variational parameter f_k determines the magnitude of the displacement of each mode, when $f_k = 0$ the displacement is zero. If we set $f_k = g_k$, the variational polaron transformation reduces to the full polaron transformation. The variational method allows us to determine an optimal value of f_k between 0 and g_k, making the transformation valid over a wide range of parameters. The effects of the polaron transformation act on the SBM can be illustrated by a double-well in the coordinate space (see Fig. 2). The polaron transformation displaces the effective potential for each local state, and further renormalizes the tunneling rate and the SBC strength. By choosing f_k properly (see below), the high-order SBC are involved in these renormalized parameters, thus the second-order perturbative calculation with the effective SBC is able to give the accurate result.

Applying the transformation to the total Hamiltonian in Eq. (1), we have

$$\tilde{H}_{tot} = U H_{tot} U^\dagger = \tilde{H}_0 + \tilde{H}_I, \tag{3}$$

where the free Hamiltonian is $\tilde{H}_0 = \tilde{H}_S + \tilde{H}_B$. The transformed system Hamiltonian is given by

$$\tilde{H}_S = \frac{\epsilon}{2}\sigma_z + \frac{\Delta_\kappa}{2}\sigma_x + \sum_k \frac{f_k}{\omega_k}(f_k - 2g_k) \tag{4}$$

and the bath Hamiltonian remains unaffected, $\tilde{H}_B = \sum_k \omega_k b_k^\dagger b_k$. The last term in Eq. (4) is a constant hence can be removed. The tunneling rate is renormalized by the expectation value of the bath displacement operator,

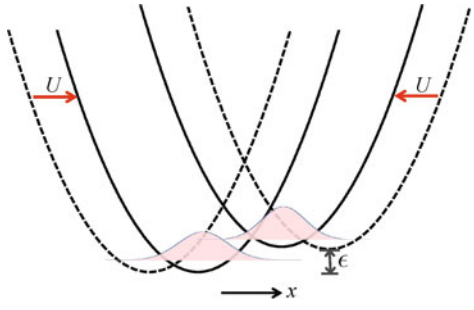

Fig. 2 Polaron effects in the SBM in the coordinate space. The dashed line illustrates the effective potentials for the local states, which are induced by the boson bath and presented as harmonic wells. The polaron transformation U displaces the potential wells (*solid line*) and renormalizes both the tunneling rate and the SBC strength.

$\Delta_\kappa = \kappa\Delta$, where

$$\kappa = \langle \cos B \rangle_{\tilde{H}_B} = \exp\left[-2\sum_k \frac{f_k^2}{\omega_k^2}\coth\left(\frac{\beta\omega_k}{2}\right)\right] \quad (5)$$

and $\langle\cdot\rangle_{\tilde{H}_B}$ represents the average over the bath canonical density matrix $\rho_B = \mathrm{e}^{-\beta\tilde{H}_B}/\mathrm{Tr}_B[\mathrm{e}^{-\beta\tilde{H}_B}]$. The transformed interaction Hamiltonian becomes

$$\tilde{H}_I = \sigma_x V_x + \sigma_y V_y + \sigma_z V_z \quad (6)$$

where

$$V_x = \frac{\Delta}{2}(\cos B - \kappa), \quad (7)$$

$$V_y = \frac{\Delta}{2}\sin B, \quad (8)$$

$$V_z = \sum_k (g_k - f_k)(b_k^\dagger + b_k). \quad (9)$$

The interaction Hamiltonian is constructed such that its thermal average is zero, $\mathrm{Tr}_B[\tilde{H}_I \exp(-\beta\tilde{H}_B)] = 0$.

Following Silbey and Harris [22, 23], we determine the optimal values for the set $\{f_k\}$ by minimizing the Gibbs-Bogoliubov–Feynman upper bound on the free energy [44–46]

$$A_B = -\frac{1}{\beta}\ln \mathrm{Tr}_{S+B}[\mathrm{e}^{-\beta\tilde{H}_0}] + \langle \tilde{H}_I \rangle_{\tilde{H}_0}, \quad (10)$$

where $\langle\,\rangle_{\tilde{H}_0}$ denotes the average over the canonical state with respect to $\tilde{H}_0$. Since $\langle \tilde{H}_I \rangle_{\tilde{H}_0} = 0$, the upper bound is solely determined by the free Hamiltonian $\tilde{H}_0$. The variational theorem states that $A_B \geqslant A_F$ where A_F is the true free energy of $\tilde{H}_{tot}$. Therefore, we seek for the minimal of A_B with respect to f_k by solving $dA_B/df_k = 0$. The minimization condition leads to

$$f_k = g_k F(\omega_k), \quad (11)$$

$$F(\omega_k) = \left[1 + \frac{\Delta_\kappa^2}{\omega_k \Lambda}\coth\left(\frac{\beta\omega_k}{2}\right)\tanh\left(\frac{\beta\Lambda}{2}\right)\right]^{-1}, \quad (12)$$

where $\Lambda = \sqrt{\epsilon^2 + \Delta_\kappa^2}$. In the continuum limit, the renormalization constant can be written as

$$\kappa = \exp\left[-2\int_0^\infty \frac{\mathrm{d}\omega}{\pi}\frac{J(\omega)}{\omega^2}F(\omega)^2\coth\left(\frac{\beta\omega}{2}\right)\right], \quad (13)$$

where the bath spectral density $J(\omega) = \pi\sum_k g_k^2\delta(\omega - \omega_k)$. Throughout the paper, we use a super-ohmic spectral density with an exponential cut-off,

$$J(\omega) \propto \gamma\omega^3\omega_c^{-2}\mathrm{e}^{-\omega/\omega_c}, \quad (14)$$

where γ is the dimensionless SBC strength. The cut-off frequency is denoted by ω_c, which governs the bath relaxation time $\tau_B \propto \omega_c^{-1}$.

Since $F(\omega)$ is also a function of κ, the set of $\{f_k\}$ must be solved self-consistently via Eqs. (11) and (12). Nevertheless, without numerical calculation, the expressions of $F(\omega)$ and κ have already shown insightful physics in two limits: (i) When the bath is slow ($\Delta \gg \omega_c$) or the SBC is weak ($\gamma \ll 1$), we find $F(\omega) \approx 0$ and $f_k \approx 0$, the polaron picture is obviously not applicative in this limit since the bath modes cannot follow the fast coherent oscillation of the system, thus the bath oscillators are barely displaced. (ii) When the bath is fast ($\Delta \ll \omega_c$) or the SBC is strong ($\gamma \gg 1$), we find $F(\omega) \approx 1$ and $f_k \approx g_k$, i.e., the full polaron transformation is recovered. Therefore, when dealing with the open system with fast bath, we can apply the full polaron transformation by setting $f_k = g_k$ for simplicity without loosing much accuracy (see Section 3.1).

3 Equilibrium distribution of the SBM via the polaron approach

This section is dedicated to study the equilibrium state of the SBM in the polaron frame, which is motivated mainly for two reasons: (i) The calculation of the equilibrium state of the SBM provides a benchmark to assess the accuracy of only the second-order perturbation theory (2nd-PT) in the polaron frames, without involving additional approximations, such as factorized initial conditions and the Born-Markov approximation which are generally invoked in the quantum master equation. This investigation can clearly demonstrate how accurate does the polaron approach depend on the bath properties, namely, the bath relaxation time and the coupling strength. (ii) Equilibrium canonical distribution in statistical mechanics assumes weak SBC, while under real physical conditions this assumption is usually invalid, thus the equilibrium statistics is generally non-canonical. By exploiting the polaron transformation with perturbation theory, an analytical treatment is advocated to study non-canonical statistics of the SBM at arbitrary temperature and for arbitrary SBC strength.

3.1 Accuracy of the perturbation theory in the polaron frame

First, we briefly introduce the second-order correction to the equilibrium state of the system in the polaron frame. The exact equilibrium RDM can be formally defined as

$$\tilde{\rho}_S = \frac{\mathrm{Tr}_B[\mathrm{e}^{-\beta\tilde{H}_{tot}}]}{\mathrm{Tr}_{S+B}[\mathrm{e}^{-\beta\tilde{H}_{tot}}]}. \quad (15)$$

In this review, the operator with a tilde denotes it is defined in the polaron frame, for example $\tilde{\rho} = U^{\dagger}\rho U$, where ρ is the density matrix in the untransformed frame. Using the Kubo identity [47, 48], the operator $\exp[-\beta\tilde{H}_{tot}]$ is expanded up to the second order in $\tilde{H}_I$ as

$$\mathrm{e}^{-\beta\tilde{H}_{tot}} \approx \mathrm{e}^{-\beta\tilde{H}_0}\Big[1 - \int_0^{\beta} \mathrm{d}\beta' \mathrm{e}^{\beta'\tilde{H}_0}\tilde{H}_I \mathrm{e}^{-\beta'\tilde{H}_0} + \int_0^{\beta}\int_0^{\beta'} \mathrm{d}\beta'\mathrm{d}\beta'' \mathrm{e}^{\beta'\tilde{H}_0}\tilde{H}_I \mathrm{e}^{-(\beta'-\beta'')\tilde{H}_0}\tilde{H}_I \mathrm{e}^{-\beta''\tilde{H}_0}\Big]. \tag{16}$$

The above expansion is similar to the Dyson expansion, with β treated as imaginary time. Since $\langle \tilde{H}_I \rangle_{\tilde{H}_0} = 0$, the leading order correction to $\tilde{\rho}_S$ is of the second order in $\tilde{H}_I$. Inserting the above expression into Eq. (15) and keeping terms up to the second order, the system equilibrium state is approximated as

$$\begin{aligned} &\tilde{\rho}_S = \tilde{\rho}_S^{(0)} + \tilde{\rho}_S^{(2)} + \ldots, \\ &\tilde{\rho}_S^{(0)} = \mathrm{e}^{-\beta\tilde{H}_S}/Z_S^{(0)}, \\ &\tilde{\rho}_S^{(2)} = \frac{A}{Z_S^{(0)}} - \frac{Z_S^{(2)}}{[Z_S^{(0)}]^2}\mathrm{e}^{-\beta\tilde{H}_S}, \end{aligned} \tag{17}$$

where

$$\begin{aligned} A = &\sum_{n,m=x,y,z}\int_0^{\beta}\int_0^{\beta'} \mathrm{d}\beta'\mathrm{d}\beta'' C_{nm}(\beta'-\beta'') \\ &\times \mathrm{e}^{-\beta\tilde{H}_S}\sigma_n(\beta')\sigma_m(\beta''), \\ Z_S^{(0)} = &\,\mathrm{Tr}_S[\mathrm{e}^{-\beta\tilde{H}_S}], \\ Z_S^{(2)} = &\,\mathrm{Tr}_S[A], \end{aligned} \tag{18}$$

and $C_{nm}(\tau) = \langle V_n(\tau) V_m \rangle_{\tilde{H}_B}$ is the imaginary-time bath correlation function. The operators in imaginary time are defined as $O(\beta) \equiv \mathrm{e}^{\beta\tilde{H}_0} O \mathrm{e}^{-\beta\tilde{H}_0}$. The expressions for the non-vanishing bath correlation functions are shown in Appendix A. The full polaron result can be conveniently obtained by setting $F(\omega) = 1$, then the only non-vanishing correlation functions are C_{xx} and C_{yy}. Furthermore, in this extremely strong coupling limit $\gamma \to \infty$, it can be seen from Eq. (13) that $\kappa \to 0$ and the system becomes incoherent since the coherent tunneling element vanishes. As a result, all of the correlation functions and the second-order corrections to $\tilde{\rho}_S$ vanish; hence the equilibrium density matrix is only determined by the energy splitting of the two local energy levels, $\tilde{\rho}_S \propto \exp(-\epsilon\beta\sigma_z/2)$. In the opposite limit, $F(\omega) = 0$ which corresponds to no transformation is performed and C_{zz} is the only non-zero correlation function.

Since the populations of the TLS are not affected by the transformation, $\mathrm{Tr}_S[\sigma_z\rho_S] = \mathrm{Tr}_S[\sigma_z\tilde{\rho}_S] \equiv \langle\sigma_z\rangle$, we can directly compare the expectation value $\langle\sigma_z\rangle$ from 2nd-PT in the original frame [$F(\omega) = 0$], the full polaron frame [$F(\omega) = 1$], and the variational polaron frame [$F(\omega)$ in Eq. (12)] with those obtained from the numerically exact imaginary-time path integral calculations. Results of the transformed zeroth-order density matrix, $\tilde{\rho}_S^{(0)}$, which depend only on the renormalized system Hamiltonian $\tilde{H}_S$, are also included.

In order to get a good perspective on the accuracy of 2nd-PT in different frames depends on the properties of the bath, we calculate the relative errors over the entire range of the bath parameters. The relative error is defined as

$$\left|\frac{\langle\sigma_z\rangle_{\mathrm{Pert}} - \langle\sigma_z\rangle_{\mathrm{PI}}}{\langle\sigma_z\rangle_{\mathrm{PI}}}\right|, \tag{19}$$

where the subscripts "Pert" and "PI" denote the perturbative calculation and path integral calculation, respectively. Figure 1 displays the respective errors of second-order perturbation in the three different frames as a function of the cut-off frequency ω_c and the coupling strength γ. As seen in Fig. 3(a), the usual 2nd-PT without transformation breaks down at large γ. It is also less accurate when the cut-off frequency is small, which corresponds to a highly non-Markovian bath. On the other hand, the 2nd-PT in the full polaron frame fails at small γ and ω_c [see Fig. 3(b)]. These two approaches provide complementary behavior as a function of the coupling strength; the full polaron method is essentially exact for large γ, while the usual 2nd-PT is exact for small γ. The variational calculation is valid over a much broader range of parameters [see Fig. 3(c)], and combines the regimes of validity of the full polaron result and the 2nd-PT in the original frame. It becomes only slightly less accurate in the slow bath regime around a narrow region of coupling strength.

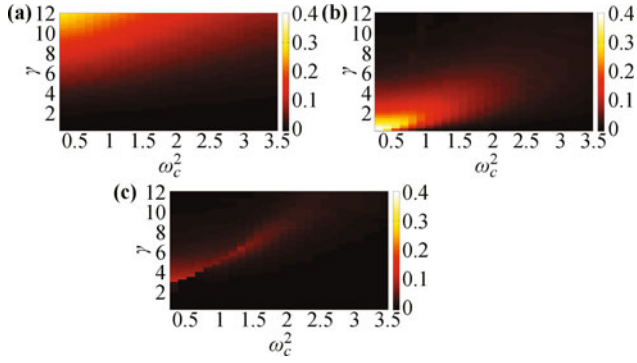

Fig. 3 At $\Delta = 3$, the relative errors of the second-order perturbation theory, compared with the exact stochastic path integral result as defined in Eq. (19), in **(a)** the original frame, **(b)** the full polaron frame, and **(c)** the variational polaron frame. Obviously, the variational polaron method is of high accuracy in the fast bath regime over the entire range of coupling strength. Reproduced from Ref. [29].

The exact numerical method we applied here as benchmark is based on imaginary-time path integrals [18]. For the SBM, following the well-known Feynman-Vernon influence functional [49]with the Hubbard-Stratonovich transformation [39], it was shown that the influence functional is unraveled by an auxiliary stochastic field. The ensuing imaginary-time evolution of the density matrix may then be interpreted as one governed by a time-dependent Hamiltonian with a stochastic field. A primary benefit of this approach is that it generates the entire RDM from one Monte Carlo simulation. Additionally, any form for the bath spectral density $J(\omega)$ can be used. The details of the numerical algorithm can be found in Ref. [18].

In the following of this paper, we will only consider the bath with large cut-off frequency such that the full polaron transformation can be safely applied. Without making ambiguity, from now on when we use the word "polaron transformation", it actually implies the "full polaron transformation" for brevity.

3.2 Non-canonical equilibrium distribution

To investigate the non-canonical statistics of the TLS at arbitrary temperature and arbitrary SBC strength, both the population and coherence of the RDM should be compared with the canonical density matrix. In particular, we use the RDM in the system eigenbasis to quantify the non-canonical statistics as well as the quantumness of the open system. The agreement of the analytical treatment based on the polaron transformation with the exact stochastic path integral result is also verified.

Different from the diagonal elements ρ_S^{11} and ρ_S^{22}, which are given above by $(1 \pm \langle\sigma_z\rangle)/2$, the off-diagonal element ρ_S^{12} in the polaron picture is more involved because the σ_z operator does not commute with the polaron transformation operator U. Nevertheless, we find

$$\rho_S^{12} = \mathrm{Tr}[\sigma_- \rho_{tot}] = \mathrm{Tr}[\tilde{\sigma}_- \tilde{\rho}_{tot}] = \mathrm{Tr}[\sigma_- \cos B \tilde{\rho}_{tot}] \quad (20)$$

indicating that ρ_S^{12} can still be obtained from $\tilde{\rho}_{tot}$, but not from $\tilde{\rho}_S$. Because of the correlation between the system and the bath, the first-order contribution of $\tilde{H}_I$ to $\exp[-\beta\tilde{H}_{tot}]$ and hence to $\tilde{\rho}_{tot}$ is already nonzero (upon thermal averaging). As such, it suffices to consider a first-order perturbation theory in imaginary time for the total density matrix in the polaron frame. With details elaborated in Ref. [30], we obtain $\rho_S^{12} \approx \rho_{S,(0)}^{12} + \rho_{S,(1)}^{12}$, with

$$\rho_{S,(0)}^{12} = -\frac{\kappa\Delta_\kappa}{2\Lambda}\tanh(\beta\Lambda/2), \quad (21)$$

$$\rho_{S,(1)}^{12} = -\sum_{n=x,y}\int_0^\beta \mathrm{d}\tau S_n(\tau)K_n(\tau). \quad (22)$$

Here $S_n(\tau) = \langle\sigma_n(\tau)\sigma_-\rangle_{\tilde{H}_S}$ and $K_n(\tau) = \langle V_n(\tau)\cos B\rangle_{\tilde{H}_B}$ are the correlation functions of the system and the bath, respectively, which are given in Appendix A.

Instead of examining all the RDM elements, a single quantity is used to characterize non-canonical statistics: the smallest possible angle θ. It is the angle rotated (in radians) on the Bloch sphere to reach the eigenstates of H_S from the diagonal representation of the RDM. As a function of the SBC strength γ for a fixed temperature, the theoretical results (solid line) are plotted in Fig. 4(a). For small values of γ, θ is small, so the RDM's diagonal representation is relatively close to that of H_S. This is expected, because for weak SBC strength, the equilibrium statistics should be canonical. As γ increases, θ increases, indicating that the RDM diagonal representation continuously and monotonously rotates away from the eigenstates of H_S. To further elucidate the continuous change in θ, an analogous angle, namely, the angle that the RDM diagonal representation should be rotated to reach the eigenstates of H_I, is also plotted with dashed line in Fig. 4(a). For large values of γ, we find $\kappa \to 0$, the SBM reduces to a pure dephasing model. Therefore, the RDM diagonal representation is seen to approach that of H_I (or σ_z), and the system equilibrium state approaches $\exp(-\epsilon\beta\sigma_z/2)$. For a varying SBC strength, either weak or strong, the 2nd-PT polaron approach and the numerically exact results agree, which confirms that our analytical treatment for the RDM off-diagonal elements performs equally well in the regime valid

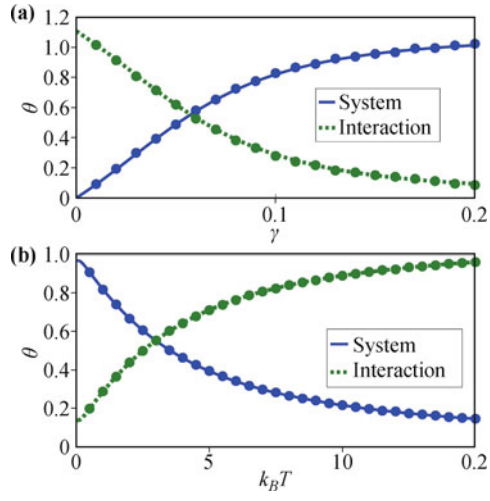

Fig. 4 **(a)** Coupling strength dependence of the angle to be rotated on the Bloch sphere to reach eigenstates of $\tilde{H}_S$ (*solid line*) or $\tilde{H}_I$ (*dashed line*) from eigenstates of equilibrium RDM, for $\beta = 1$, $\epsilon = 0.5$, and $\omega_c = 5$ (in units of Δ). **(b)** Temperature dependence of the angle to be rotated on the Bloch sphere to reach eigenstates of $\tilde{H}_S$ (*solid line*) or $\tilde{H}_I$ (*dashed line*) from eigenstates of equilibrium RDM, for $\gamma = 0.1$, $\epsilon = 0.5$, and $\omega_c = 5$. Solid dots are numerically exact stochastic path integral results. Reproduced from Ref. [30].

for treating the RDM diagonal elements.

The equilibrium RDM considered here reminds us the preferred basis discussed in decoherence dynamics [50]: An equilibrium RDM is an asymptotic result of quantum dissipation. Due to this interesting connection, the particular diagonal representations of RDM as a result of the non-canonical statistics can also be understood as a remarkable outcome of nature's superselection in open quantum systems [51–54].

The temperature dependence of non-canonical statistics at a fixed intermediate SBC strength γ is depicted in Fig. 4(b). For temperature lower than $k_BT = 1$, the RDM diagonal representation is further rotated from that of H_S (solid line) but becomes closer to that of H_I (dashed line). Therefore, the non-canonical statistics becomes more pronounced when temperature decreases. When temperature increases, the deviation angle continuously changes in opposite directions, showing that the RDM diagonal representation gradually moves away from the eigen-representation of H_I but smoothly approaches that of H_S. Numerically exact Monte Carlo simulation results (solid dots) are also presented in Fig. 4(b), further supporting our theory.

4 Polaron transformed Redfield equation

Besides solving the equilibrium states, the polaron transformation is also a powerful tool to study the dynamics of open quantum systems at strong coupling via the second-order master equation. Applying the polaron method to study the dynamics of open quantum systems was first proposed by Grover and Silbey [24], and it has gained a renewed attention due to the recent interest in coherent energy transfer in light harvesting systems [25–27] and has been extended to study non-equilibrium quantum system [33, 34], which we will introduce in Sec.V. For non-equilibrium steady state, the non-Markovian effect is less significant so we will adopt the secular and Markov approximation.

After the transformation, the system is dressed by polaron, then the master equation is obtained by applying perturbation theory to the transformed system-bath interaction. This approach extends the regime of validity of the quantum master equation to stronger SBC, provided that the tunneling matrix elements are small compared to the bath cut-off frequency ($\Delta < \omega_c$).

In this subsection, we use the SBM as example to introduce the PTRE approach. For a multi-level system, the PTRE can be generalized straightforwardly following the same procedure [28]. The Hamiltonian of the SBM after the full polaron transformation is given in Eq. (3) with $f_k = g_k$. The strength of the SBC is effectively weakened by the polaron transformation. Specifically, $\tilde{H}_I$ is of the order of bath fluctuation and its thermal average is zero, hence $\tilde{H}_I$ is a reliable perturbative parameter. Based on this consideration, the Born–Markov approximation is applied to derive the PTRE for SBM in the Schrodinger picture:

$$\frac{\mathrm{d}\tilde{\rho}_S(t)}{\mathrm{d}t} = -\mathrm{i}[\tilde{H}_S, \tilde{\rho}_S(t)] - \int_0^\infty \mathrm{d}s \mathrm{Tr}_B\{[\tilde{H}_I, [\tilde{H}_I(-s), \tilde{\rho}_S(t)\otimes\rho_B]]\}, \quad (23)$$

which can be further written as

$$\frac{\mathrm{d}\tilde{\rho}_S}{\mathrm{d}t} = -\mathrm{i}[\tilde{H}_S, \tilde{\rho}_S] - \sum_{\alpha,\beta=z,\pm}[\Gamma^+_{\alpha\beta}\tau_\alpha\tau_\beta\tilde{\rho}_S + \Gamma^-_{\beta\alpha}\tilde{\rho}_S\tau_\beta\tau_\alpha - \Gamma^-_{\beta\alpha}\tau_\alpha\tilde{\rho}_S\tau_\beta - \Gamma^+_{\alpha\beta}\tau_\beta\tilde{\rho}_S\tau_\alpha]. \quad (24)$$

Here we use a new set of Pauli operators τ_α with respect to the eigenbasis of the Hamiltonian $\tilde{H}_S = \Lambda\tau_z$:

$$\tau_z = |+\rangle\langle+| - |-\rangle\langle-|, \quad (25)$$

$$\tau_+ = |+\rangle\langle-|, \ \tau_- = |-\rangle\langle+|. \quad (26)$$

The eigenbasis are defined with the local basis $|1\rangle$ and $|2\rangle$ as

$$|+\rangle = \cos\frac{\theta}{2}|1\rangle + \sin\frac{\theta}{2}|2\rangle, \quad (27)$$

$$|-\rangle = \sin\frac{\theta}{2}|1\rangle - \cos\frac{\theta}{2}|2\rangle, \quad (28)$$

where $\tan\theta = \Delta_\kappa/\epsilon$. The dissipation rates $\Gamma^\pm_{\alpha\beta}$ are related to the half-side Fourier transformation of the bath correlation functions

$$\Gamma^\pm_{\alpha\beta} = \frac{\Delta^2}{4}\int_0^\infty \mathrm{d}t\,\langle\xi_\alpha(\pm t)\,\xi_\beta(0)\rangle, \quad (29)$$

with

$$\xi_z(t) = \sin\theta[\cos B(t) - \kappa], \quad (30)$$

$$\xi_\pm(t) = -\mathrm{e}^{\pm\mathrm{i}\Lambda t}\{\cos\theta[\cos B(t) - \kappa] \mp \mathrm{i}\sin B(t)\}. \quad (31)$$

Therefore, the steady state of the system can be easily obtained from Eq. (24) by solving $\mathrm{d}\tilde{\rho}_S/\mathrm{d}t = 0$.

4.1 Steady states and equilibrium distribution

The expectations of the operators τ_α in the steady state, which contain all the information of the TLS in SBM are displayed in Fig. 5. The dependence of the population difference $\langle\tau_z\rangle$ on the coupling strength γ is plotted with the blue solid line. It is found that the steady

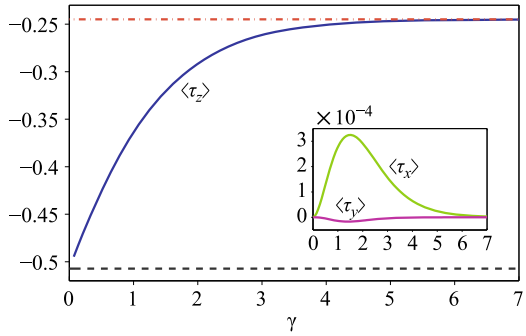

Fig. 5 The steady state of TLS as a function of the SBC strength γ. The steady states of the PTRE follow the canonical distribution in the polaron transformed basis, which rotates with the coupling strength γ. In the weak coupling limit, the system steady state is the canonical distribution in the eigen basis (*black dash line*); while in the strong coupling limit, the steady state is the canonical distribution in the localized basis (*red dot-dash line*). The inset shows the coherent term of the steady state, which is small in the polaron transformed basis. We choose the parameters in units of Δ: $\epsilon = 0.5$, $\omega_c = 5$ and $\beta = 1$. Reproduced from Ref. [34].

state RDM obtained from the PTRE coincides with the zeroth-order perturbation result of the equilibrium state in Eq. (17). The steady state distribution of the TLS follows the Boltzmann distribution with respect to the eigenbasis in the polaron frame

$$\langle \tau_z \rangle = -\tanh(\frac{1}{2}\beta\Lambda). \tag{32}$$

It is reduced to the canonical distribution with respect to the eigenbasis of H_S as $\lim_{\gamma\to 0}\langle\tau_z\rangle = -\tanh[\beta\sqrt{\epsilon^2+\Delta^2}/2]$, and is reduced to $\lim_{\gamma\to\infty}\langle\tau_z\rangle = -\tanh[\beta\epsilon/2]$ in the strong coupling limit, which is the Boltzmann distribution in the local basis $|1\rangle$ and $|2\rangle$.

4.2 Validity of the PTRE

For an unbiased two-level system, we compare the result

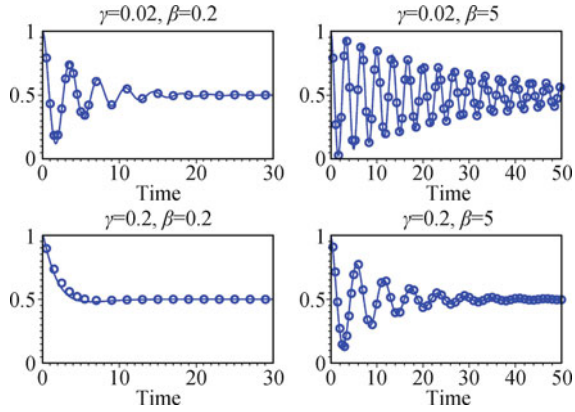

Fig. 6 Time evolution of the population dynamics of the state $|1\rangle$ calculated from the PTRE Eq. (24) (*symbols*) and the time-convolutionless second-order polaron master equation used in Ref. [55] (*solid lines*). The parameters used are $\epsilon_1 - \epsilon_2 = 0$, $\Delta = 2$ and $\omega_c = 3$. Reproduced from Ref. [28].

obtained from the above PTRE Eq. (24) with that from the time-convolutionless second-order polaron master equation without the secular and Markov approximations [55]. The results are plotted in Fig. 6, they show remarkably good agreements for different temperature and coupling strength. Moreover, as shown below, the PTRE recovers the Redfield equation in the weak coupling limit and the Fermi's golden rule (or Förster theory) in the strong coupling limit.

4.3 Weak and strong coupling limits

In the weak coupling limit, we have $\kappa \approx 1$, thus the eigenbasis $|\pm\rangle$ of the polaron transformed Hamiltonian $\tilde{H}_S$ become the eigenbasis of $H_S = \frac{\epsilon}{2}\sigma_z + \frac{\Delta}{2}\sigma_x$. In this case the master equation in Eq. (24) with secular approximation is reduced to the Redfield equation

$$\frac{\mathrm{d}\rho_S^{++}}{\mathrm{d}t} = -\Gamma\left[1+N\left(\Lambda_0\right)\right]\rho_S^{++} + \Gamma N\left(\Lambda_0\right)\rho_S^{--}, \tag{33}$$

$$\frac{\mathrm{d}\rho_S^{+-}}{\mathrm{d}t} = -\mathrm{i}\Lambda_0\rho_S^{+-} - \Gamma[\frac{1}{2}+N\left(\Lambda_0\right)]\rho_S^{+-}, \tag{34}$$

where $\Gamma = \frac{1}{2}J\left(\Lambda_0\right)\sin^2\theta$, $\Lambda_0 = \sqrt{\epsilon^2+\Delta^2}$ and $N\left(\omega\right) = 1/\left[\exp\left(\beta\omega\right)-1\right]$. In the strong coupling limit, the coherence is quickly destroyed by dissipation, thus we only need to consider the equations of the population. Additionally, $\kappa \approx 0$ for large γ, i.e., the eigenbasis of $\tilde{H}_S$ coincide with the local basis $|1\rangle$ and $|2\rangle$. As a result, Eq. (24) becomes a kinetic equation governing the population dynamics, which can be written as

$$\frac{\mathrm{d}\rho_S^{11}}{\mathrm{d}t} = -\Gamma_{11}\rho_S^{11} + \Gamma_{12}\rho_S^{22}, \tag{35}$$

where

$$\Gamma_{11} = \frac{1}{2}\kappa^2\Delta^2\int_0^\infty \mathrm{d}\tau\Re\left[\mathrm{e}^{\mathrm{i}\epsilon\tau}\left(\mathrm{e}^{Q(\tau)}-1\right)\right], \tag{36}$$

$$\Gamma_{12} = \frac{1}{2}\kappa^2\Delta^2\int_0^\infty \mathrm{d}\tau\Re\left[\mathrm{e}^{-\mathrm{i}\epsilon\tau}\left(\mathrm{e}^{Q(\tau)}-1\right)\right], \tag{37}$$

and

$$Q\left(\tau\right) = \int_0^\infty \mathrm{d}\omega\frac{J\left(\omega\right)}{\pi\omega^2}[\cos\left(\omega\tau\right)\coth\left(\beta\omega/2\right) - \mathrm{i}\sin\left(\omega\tau\right)]. \tag{38}$$

The above transition rates Γ_{11} and Γ_{12} are the same as predicted from the Fermi's golden rule. In summary, the PTRE smoothly connects the weak and strong limits, and provides a useful tool to study the intermediate coupling region where there is usually no reliable approximation method.

5 Applications of PTRE to exciton diffusion, heat transport and energy transfer

The PTRE cannot only be used in calculating the steady state and the dynamics of equilibrium systems, but also apply to non-equilibrium problems such as exciton diffusion in disordered system, heat transport through quantum dot and energy transfer in heat engine model. The steady states of these non-equilibrium processes are usually of special interests as they are closely related to the measurable quantities in experiments. The PTRE is a proper tool to study these problems in order to bridge the gap between the standard Redfield equation in weak coupling regime and the Fermi's golden rule or the noninteracting-blip approximation (NIBA) in strong coupling regime.

5.1 Coherent exciton transport in disordered systems

Quantum transport in disordered systems governs a host of fundamental physical processes including the efficiency of light harvesting systems, organic photovoltaics, conducting polymers, and J-aggregate thin films [56–65]. The PTRE approach to quantum transport allows us to bridge coherent band-like transport governed by the Redfield equation to incoherent classical hopping transport described by the Fermi's golden rule. The results reveal that a non-monotonic dependence of the diffusion coefficient can be observed as a function of temperature and system-phonon coupling strength.

The system is extended from single TLS to a tight binding model, described by the Anderson Hamiltonian (see Fig. 7)

$$H_S = \sum_n \epsilon_n |n\rangle \langle n| + \sum_{m\neq n} J_{mn} |m\rangle \langle n|, \tag{39}$$

where $|n\rangle$ denotes the site basis and J_{mn} is the electronic coupling between site m and site n. Here, we consider one dimensional system with nearest-neighbor coupling such that $J_{mn} = J(\delta_{m,n+1} + \delta_{m+1,n})$. The static disorder is introduced by taking the site energies ϵ_n to be independent, identically distributed Gaussian random variables characterized by their variance $\sigma_n^2 = \overline{\epsilon_n \epsilon_n}$. The overline is used throughout to denote the average over static disorder. We assume that each site is independently coupled to its own phonon bath in the local basis. Thus,

$$H_B = \sum_{nk} \omega_{nk} b_{nk}^\dagger b_{nk}, \tag{40}$$

$$H_I = \sum_{nk} g_{nk} |n\rangle \langle n| (b_{nk}^\dagger + b_{nk}), \tag{41}$$

where ω_{nk} and $b_{nk}^\dagger(b_{nk})$ are the frequency and the creation (annihilation) operator of the kth mode of the bath attached to site n with coupling strength g_{nk}, respectively.

Applying the full polaron transformation and following the same procedure in Section 4, a second-order PTRE in terms of the transformed SBC with Markov and secular approximations is given by

$$\frac{\mathrm{d}\tilde{\rho}_{\nu\nu}(t)}{\mathrm{d}t} = \sum_{\nu'} R_{\nu\nu,\nu'\nu'} \tilde{\rho}_{\nu'\nu'}(t), \tag{42}$$

$$\frac{\mathrm{d}\tilde{\rho}_{\mu\nu}(t)}{\mathrm{d}t} = (-i\omega_{\nu\mu} + R_{\mu\nu,\mu\nu})\tilde{\rho}_{\mu\nu}(t), \ \nu \neq \mu. \tag{43}$$

The Greek indices denote the eigenstates of the polaron transformed system Hamiltonian, i.e., $\tilde{H}_S |\mu\rangle = \tilde{E}_\mu |\mu\rangle$ and $\omega_{\mu\nu} = \tilde{E}_\mu - \tilde{E}_\nu$. The Redfield tensor $R_{\mu\nu,\mu'\nu'}$ describes the phonon-induced relaxation, the detailed expressions are given in Appendix B. For the transport properties studied here, only the population dynamics is needed which is invariant under the polaron transformation since $\tilde{\rho}_{nn}(t) = \rho_{nn}(t)$. In the presence of both disorder and dissipation, we find empirically that after an initial transient time approximately proportional to $J^3\beta/\gamma$, the mean square displacement $\overline{\langle R^2(t)\rangle} = \overline{\sum_n n^2 \rho_{nn}(t)}$ grows linearly with time, where the origin is defined such that $\overline{\langle R^2(0)\rangle} = 0$. Within the timescale of the simulations, the number of sites is sufficient such that no significant boundary effect is observed. Then the diffusion constant D can be defined as $\lim_{t\to\infty} \overline{\langle R^2(t)\rangle} = 2Dt$.

The effect of the dissipation strength on the diffusion constant is revealed as a non-monotonic dependence on D as a function of γ in Fig. 8, which is consistent with the studies using the Haken–Strobl model [66, 67]. The dissipation destroys the phase coherence that gives rise to Anderson localization in one-dimensional disordered system, allowing for transport to occur. Therefore, in the weak coupling regime, the transport coefficient D increases linearly with γ, which is apparent from the Redfield tensor $R_{\mu\nu,\mu'\nu'}$. In the opposite regime of strong coupling, the dissipation strength effectively acts as

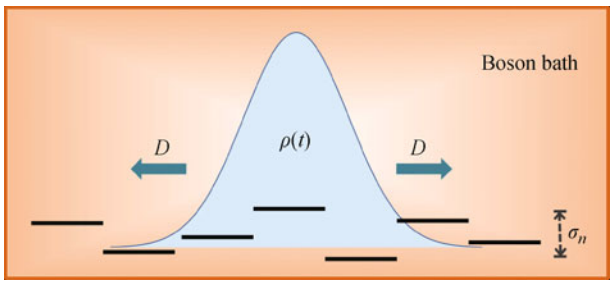

Fig. 7 Illustration of the diffusion of a single excitation in one dimensional system with static disorder and local bosonic noise.

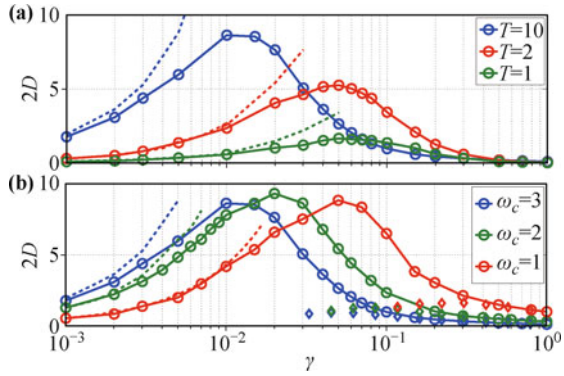

Fig. 8 The diffusion constant as a function of the dissipation strength γ. The dashed lines display the corresponding results from the secular Redfield equation, while diamond symbols depict the results of the Fermi's golden rule rates. **(a)** Results for different temperatures and a fast bath $\omega_c = 3$. **(b)** Results for different cut-off frequencies and $T = 10$. The electronic coupling $J = 1$ sets the energy scale. Reproduced from Ref. [28].

classical friction that impedes the transport leading D to behave as a decreasing function of γ. Thus the coherence generated between sites is quickly destroyed and the quantum transport reduces to a classical hopping dynamics between neighboring sites. The interplay between static disorder and dissipation thus gives rise to an optimal dissipation strength for transport. In Fig. 8(a), it is seen that the maximal diffusive rate both increases and shifts to smaller coupling strengths as the temperature increases, since thermal fluctuations also assist the quantum system to overcome the localization barriers in the weak coupling regime. For comparison, we also include the results from the standard secular Redfield equation in the weak coupling regime. For small γ and T, the secular Redfield equation provides a reliable description of the transport properties but starts to breakdown as γ (or T) increases leading to an unphysical $D \propto \gamma$.

Figure 8(b) depicts D as a function of γ for different bath cut-off frequencies. It is found that the large γ scaling of D is highly dependent on the relaxation time of the bath. For a fast bath, the rates decrease approximately as $1/\gamma$. However, as the bath frequency decreases, a transition from the $1/\gamma$ dependence to $1/\sqrt{\gamma}$ dependence is observed. This can be rationalized by noting that in the high temperature and strong damping regime, the dynamics is incoherent and can be described by classical hopping between nearest neighbors. Then, the hopping rate between sites m and n is accurately determined from Fermi's golden rule,

$$k_F(\Delta_{mn}) = J_{mn}^2 \kappa_{mn}^2 \Re \int_{-\infty}^{\infty} \mathrm{d}t \mathrm{e}^{\mathrm{i}\Delta_{mn}t}[\mathrm{e}^{g(t)} - 1], \quad (44)$$

and

$$g(t) = 2\int_0^{\infty} \mathrm{d}\omega \frac{J(\omega)}{\pi\omega}\left[\cos(\omega t)\coth(\beta\omega/2) - \mathrm{i}\sin(\omega t)\right], \quad (45)$$

where $\Delta_{mn} = \epsilon_m - \epsilon_n$ is the activation barrier. In the slow bath limit, the above expression reduces to the Marcus rate

$$k_M(\Delta) \approx \frac{\pi}{2} J^2 \sqrt{\frac{\beta}{\gamma\omega_c^3}} \exp\left[-\frac{\beta(\pi\Delta - 4\gamma\omega_c^3)^2}{16\pi\gamma\omega_c^3}\right], \quad (46)$$

which captures the correct $1/\sqrt{\gamma T}$ dependence of the rate. Defining the energy transfer time as the inverse of the rate, $\tau_F(\Delta) = 1/k_F(\Delta)$, static disorder can be introduced by averaging $\tau_F(\Delta)$ over the Gaussian distribution of static disorder: $\overline{\tau_F} = \int \mathrm{d}\Delta P(\Delta)\tau_F(\Delta)$ where $P(\Delta) = (\sigma'\sqrt{2\pi})^{-1}\exp(-\Delta^2/2\sigma'^2)$ and $\sigma'^2 = \overline{\Delta_{mn}^2} = 2\sigma^2$. The disorder-averaged golden rule rate can then be obtained using $\overline{k_F} = 1/\overline{\tau_F}$ and is plotted in Fig. 8(b). While it is seen to capture the correct scaling of D in the overdamped regime, it significantly underestimates the transport in the small and intermediate damping regimes. As the dynamics becomes more coherent, the classical hopping rate between sites provides a qualitatively incorrect description of the transport.

5.2 Non-equilibrium heat transfer through quantum dot

In presence of multiple baths with different temperatures, non-equilibrium transport phenomena can also be studied using the PTRE. For typical energy transport far from equilibrium, two baths should be included with a temperature bias, as shown in Fig. 9. The TLS with Hamiltonian H_S in Eq. (1) couples to the two baths by

$$H_I = \sigma_z \sum_{k;v=L,R} g_{k,v}(b_{k,v}^{\dagger} + b_{k,v}), \quad (47)$$

where $b_{k,v}^{\dagger}$ ($b_{k,v}$) creates (annihilates) one boson of mode k in the vth bath. The Hamiltonian of the left (L) and right (R) baths is given by $H_B = \sum_{k;v=L,R}\omega_{k,v}b_{k,v}^{\dagger}b_{k,v}$. This non-equilibrium spin-boson model (NESB) has been used to describe the electromagnetic transport through superconducting circuits [68], photonic waveguides with

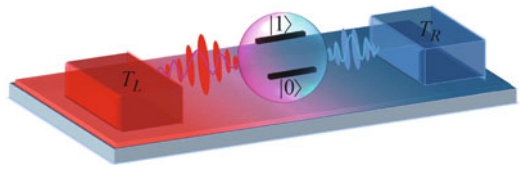

Fig. 9 Schematic illustration of the non-equilibrium spin-boson model composed by central two-level nano-device connecting to two separate bosonic baths with temperature T_L and T_R respectively. Reproduced from Ref. [33].

a local impurity [69], phononic energy transfer [70–74] and Caldeira–Leggett model [75] in phononics [76], Kondo physics and non-equilibrium phase transitions [77, 78] in the field of condense matter physics, and even exciton transfer embedded in the photosynthetic complexes [10, 60, 79–81]. Moreover, as a minimal prototype, it provides crucial insights into the optimal design and potential applications of low-dimensional nano-devices.

The PTRE approach provides a unified interpretation of several observations, including coherence-enhanced heat flux and negative differential thermal conductance (NDTC). Despite many approaches have been proposed to explore energy transfer in NESB, each approach has limitations. Typically, the Redfield equation only applies in the weak spin-boson coupling regime [72, 74], whereas the non-equilibrium version of the noninteracting-blip approximation (NIBA) equation applies in the strong spin-boson coupling regime.

Combining the polaron transformation and the counting field [74, 82], we obtain the energy flux as

$$\mathcal{J} = \frac{\Delta_\kappa^2}{8\pi}\int_{-\infty}^{\infty} \mathrm{d}\omega\omega[C_e(0,\omega) + \frac{\phi_o(\Delta_\kappa)C_o(-\Delta_\kappa,\omega)+\phi_o(-\Delta_\kappa)C_o(\Delta_\kappa,\omega)}{\phi_o(\Delta_\kappa)+\phi_o(-\Delta_\kappa)}], \quad (48)$$

where $C_{e(o)}(\omega,\omega')$ describes that when the TLS releases energy ω by relaxing from the excited state to the ground one, the right bath absorbs energy ω' and the left one obtains the left $\omega-\omega'$ if $\omega>\omega'$ or supply the compensation if $\omega<\omega'$. And $C_{e(o)}(-\omega,\omega')$ describes similar dynamical processes for the TLS jumping from the ground state to the exciting one. While $\phi_{e(0)}(\omega)$ is the summation behavior of these corresponding microscopic processes. The details of the functions $\phi_{o(e)}$ and $C_{o(e)}$ can be found in Appendix C. Different from the single bath SBM case, here the renormalization κ is actually a product of the ones from each bath: $\kappa=\kappa_L\kappa_R$.

In the weak coupling limit, the renormalization factor is simplified to $\kappa\approx 1$, then the unified energy flux reduces to the resonant energy transfer expression

$$\mathcal{J}_w = \frac{\Delta}{2}\frac{J_L(\Delta)J_R(\Delta)(n_L-n_R)}{J_L(\Delta)(1+2n_L)+J_R(\Delta)(1+2n_R)}, \quad (49)$$

with the average phonon number $n_v=n_v(\Delta)$ of the vth bath, which is consistent with previous results of the Redfield approach [72, 74]. In the strong coupling limit, multiple bosons are excited from baths, and both the renormalization factor κ and the eigen-energy gap of the TLS Δ_κ become zero. Hence, the energy flux can be finally expressed as

$$\mathcal{J}_w = \frac{\Delta^2}{8\pi}\int_{-\infty}^{\infty}\mathrm{d}\omega\omega C_L(-\omega)C_R(\omega), \quad (50)$$

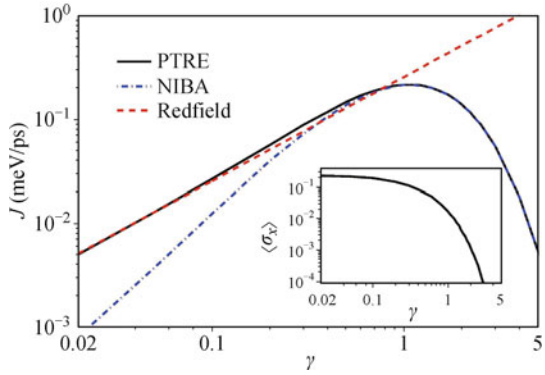

Fig. 10 The energy flux and quantum coherence represented by $\langle\sigma_x\rangle$, as functions of the coupling strength. The solid black line is from the PTRE, which unifies the Redfield result at the weak coupling (*the red dashed line*) and the NIBA result at the strong coupling (*the dot-dashed blue line*). The deviation of the unified energy flux from the NIBA result at small γ is characterized by the quantum coherence σ_x (inset). Parameters are given by $\epsilon=0$, $\Delta=5.22$ meV, $\omega_c=26.1$ meV, $T_L=150$ K and $T_R=90$ K. Reproduced from Ref. [33].

with the probability density of the vth bath $C_v(\omega)$ correctly recovering the non-equilibrium NIBA result.

The energy flux of Eq. (48) is plotted in Fig. 10, which first shows linear increase with the SBC in the weak regime, consistent with the Redfield. After reaching a maximum, the energy flux decreases monotonically in the strong coupling regime, and coincides with the NIBA result. The discrepancy of the NIBA and our PTRE is due to the improper ignorance of quantum coherence σ_x of the TLS in NIBA. This coherence term describes the effective tunneling within TLS so that it enhances the energy transfer compared to the NIBA that ignores it. Therefore, we conclude that the unified energy flux expression of Eq. (48) provides a comprehensive interpretation for energy transfer in NESB, because the fluctuation-decoupling scheme not only describes the coherent SBC from the weak to strong coupling regime, but also correctly captures the coherence within the TLS.

For the NDTC, the non-equilibrium NIBA scheme predicts its appearance in the strong coupling for NESB, whereas the Redfield scheme predicts its absence in the weak coupling. The NDTC can also be investigated by the PTRE to identify its absence over the wide range of temperature bias, even in the intermediate and strong coupling regimes, which correct the previous observation of NDTC under the NIBA in the classical limit. By tuning one bath temperature, NDTC is absent across a wide range of the temperature bias in the NESB model even in the strong SBC limit. It should also be noted, if we change two temperatures simultaneously, NDTC can still occur in NESB. The detail discussion about the NDTC via PTRE can be found in reference [33].

5.3 Energy transfer via three-level heat engine model

Taking a three-level system as a generic theoretical model, many interesting mechanisms can be well demonstrated and understood. Recently, the sunlight-induced exciton coherence is studied in a V-configuration three-level model [83, 84]. An interesting idea is to consider the energy transfer process from the perspective of heat engine [85]. For example, the coherence introduced by an auxiliary energy level can enhance the heat engine power [86, 87]. The early work considering a three-level maser model as a Carnot engine was carried out by Scovil and Schulz-DuBois [88, 89], yielding the heat engine efficiency η_0 and its relation with the Carnot efficiency. Later papers elaborately reexamined the dynamics of this model by the Lindblad master equation and showed that the thermodynamic efficiency η_0 is achieved when the output light-field is strongly coupled with the system [90–92].

We consider the energy transfer process in the three-level system illustrated in Fig. 11. The site energy of the ground state $|0\rangle$ is set to zero. The two excited energy levels $|1\rangle$ and $|2\rangle$ form a TLS, the Hamiltonian of which is the same as H_S in Eq. (1). The energy transfer takes place in the single excitation subspace: The three-level system is firstly excited to state $|1\rangle$ by a photon field, then the excitation is transferred to state $|2\rangle$ through Δ (mediated by phonon modes), and finally the excitation decays to the ground state $|0\rangle$ via spontaneous radiation. The pumping and trapping processes are modeled by the interaction with the two independent photon baths, which are coupled separately with two transitions $|0\rangle \leftrightarrow |1\rangle$ and $|0\rangle \leftrightarrow |2\rangle$. The Hamiltonian of the photon baths and their interactions with the three-level system are given by

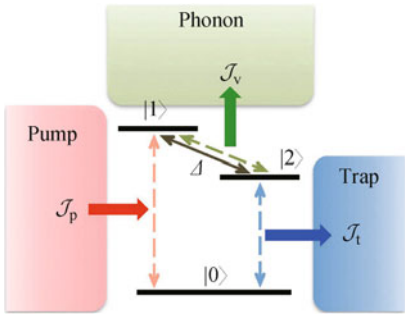

Fig. 11 The system is modeled by a three-level system: its ground state $|0\rangle$ and the excited state $|1\rangle$ ($|2\rangle$) is coupled with the pumping (trapping) bath; the excited states $|1\rangle$ and $|2\rangle$ are diagonal-coupled with the phonon bath; the internal transition strength between $|1\rangle$ and $|2\rangle$ is characterized by Δ. The energy fluxes $\mathcal{J}_p$, $\mathcal{J}_v$ and $\mathcal{J}_t$ describe the energy exchange rate of the system with the pumping, the phonon and the trapping baths, respectively. The flux into the system is defined as the positive direction. Reproduced from Ref. [34].

$$H_p = \sum_k \omega_{pk} a_{pk}^\dagger a_{pk} + (g_{pk} a_{pk}^\dagger |0\rangle\langle 1| + \text{h.c.}), \tag{51}$$

$$H_t = \sum_k \omega_{tk} a_{tk}^\dagger a_{tk} + (g_{tk} a_{tk}^\dagger |0\rangle\langle 2| + \text{h.c.}), \tag{52}$$

where ω_{ik} $(i = p, t)$ is the eigen frequency of the bath mode described by the creation (annihilation) operator $a_{ik}^\dagger$ (a_{ik}), and its coupling strength to the excited state is g_{ik}. We note that the rotating wave approximation is applied in the system-bath interaction term. A phonon bath with creation and annihilation operators $b_k^\dagger$ and b_k of the bath mode ω_{vk} is coupled to the TLS via diagonal interaction with the coupling strength of f_k. Thus, the phonon part is described by

$$H_v = \sum_k \omega_{vk} b_k^\dagger b_k + (|1\rangle\langle 1| - |2\rangle\langle 2|) \sum_k (f_k b_k^\dagger + \text{h.c.}). \tag{53}$$

The steady state of the three-level system can be easily obtained from PTRE and the steady state energy fluxes defined are straightforwardly given as

$$\mathcal{J}_p = \epsilon_1 \gamma_p [n_p \rho_{00} - (n_p + 1)\rho_{11}] - \frac{\Delta \gamma_p}{2}(n_p + 1)\Re[\rho_{12}], \tag{54}$$

$$\mathcal{J}_t = \epsilon_2 \gamma_t [n_t \rho_{00} - (n_t + 1)\rho_{22}] - \frac{\Delta \gamma_t}{2}(n_t + 1)\Re[\rho_{12}], \tag{55}$$

where the steady state elements of RDM is denoted by $\rho_{ij} = \langle i|\rho_S(\infty)|j\rangle$ for brevity, γ_i and n_i are the corresponding decay rate and average photon number for the ith bath. In Fig. 12 we present the dependence of energy fluxes on the coupling strength γ. In the extreme case that the system bath coupling is switched off ($\gamma = 0$), there is no loss of excitation energy, which results in $|\mathcal{J}_p| = |\mathcal{J}_t|$, suggesting the input energy flux from the pump completely flows into the trap through the three-level system. When the coupling turns on, a portion of energy flux leaks into the phonon bath thus $|\mathcal{J}_p| > |\mathcal{J}_t|$. Both the pumping and trapping energy fluxes reach their optimal values in the intermediate coupling region and decrease to zero when the coupling strength is strong.

The energy transfer efficiency is defined as $\eta \equiv |\mathcal{J}_t/\mathcal{J}_p|$. When the coupling strength $\gamma = 0$, the energy transfer efficiency $\eta = 1$ because there is no loss of energy flux. When the coupling strength gradually increases, the efficiency decreases. However, after reaching its minimum value, the efficiency starts to rise with γ, which is shown in Fig. 12(a). The increase of efficiency assisted by noise was studied extensively in the context of energy transfer in light-harvesting systems [93, 94]. As we further increase γ, the efficiency grows beyond the

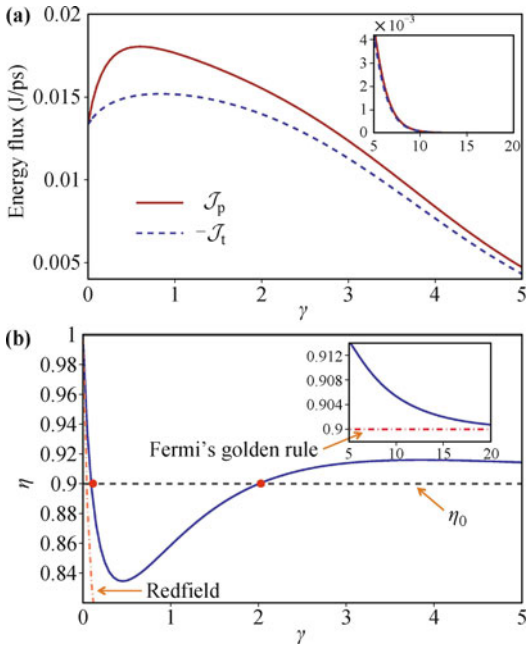

Fig. 12 **(a)** The steady state pumping (*red solid line*) and trapping (*blue dashed line*) energy fluxes versus γ. Both fluxes show a maximal value in the weak coupling case and then quickly decreases to zero when γ increases. **(b)** The steady states efficiency η is plotted with blue solid line as a function of γ. The dashed line indicates the strong coupling limit η_0. The results given by the Redfield equation and the Fermi's golden rule are shown with the dashed-dot lines. The strong coupling regions are plotted in the insets. We choose the parameters in units of Δ: $\epsilon = 0.5$, $\omega_c = 5$, $\beta_v = 1$, $\beta_p = 0.02$, $\beta_t = 1$, and $\gamma_p = \gamma_t = 0.01$. Reproduced from Ref. [34].

strong coupling limit η_0 and then gradually approaches this limit from above. The strong coupling region is plotted in the inset of Fig. 12(a).

It is interesting to notice that the first term on the right side of Eqs. (54) and (55) depends only on the populations of the three-level system, and the second term represents the contribution of the off-diagonal terms (coherence in the local basis). In the strong coupling limit, the steady state coherence in the local bases ρ_{12} vanishes, then the efficiency is completely determined by the populations:

$$\eta \approx -\frac{\epsilon_2\gamma_t[(n_t+1)\rho_{22}-n_t\rho_{00}]}{\epsilon_1\gamma_p[(n_p+1)\rho_{11}-n_p\rho_{00}]} = \frac{\epsilon_2}{\epsilon_1}. \tag{56}$$

This result indicates that when the coherence is negligible due to the strong system-phonon coupling, the energy transfer efficiency η approaches η_0, which is consistent with the key result of Ref. [91]. We notice that Eq. (56) shows that the net rate of pumping one excitation to $|1\rangle$ equals to the net rate of trapping one excitation from $|2\rangle$ to $|0\rangle$. When the coupling strength decreases, the efficiency is generally related to the phonon bath induced coherence of the excited states [95]. If we require the system outputs positive energy, i.e., $\gamma_t(n_t+1)\rho_{22} > \gamma_t n_t\rho_{00}$, then $\Re[\rho_{12}] > 0$ leads to the result $\eta > \eta_0$ and vise versa.

In the local basis, the population and coherence are coupled with each other due to the polaron effects: The population inversion happens when $\Re[\rho_{12}] < 0$ [Fig. 12(b)], hence $\eta < \eta_0$. We plot the population difference between states $|1\rangle$ and $|2\rangle$ in Fig. 12(b). In the intermediate coupling region indicated between the two red dots, the steady state population satisfies $\rho_{11} < \rho_{22}$ (the effective temperature associates with these two states is positive), the corresponding efficiency η is less then η_0 as shown in Fig. 12(a). On the contrary, outside this intermediate region, i.e., when the coupling is either very weak or very strong, the populations are inverted $\rho_{11} > \rho_{22}$ (the effective temperature is negative); meanwhile η increases beyond η_0.

As we discussed in Section 3, the non-negligible SBC strength can induce the non-canonical equilibrium states, which will further affects the heat engine performance. In this section we show the PTRE is also powerful tool to evaluate the performance of a three-level heat engine model beyond the weak coupling limit. In particular, the non-negligible system-bath entanglement not only modifies the steady state, resulting in population inversion, but also introduces a finite steady state coherence that optimizes the energy transfer flux and efficiency. Remarkably, there exists a quantitative relationship between the efficiency and the steady-state coherence, which in turn is proportional to the degree of population inversion. Taking into account of the behavior of both the flux and efficiency, we are able to optimize coupling and temperature in designing optimal artificial energy transfer systems.

6 Summary

In this review article, we systematically introduce the polaron transformation approach to describe non-canonical equilibrium distribution and non-equilibrium steady states in the open quantum system. By applying the polaron transformation, the open system of interest is dressed by the surrounded environment which is described by a set of displaced harmonic modes. The residue coupling between the polaron transformed system and the bath is thus suppressed to the weak coupling regime, even though the SBC in the original frame of reference is strong. Such advantages give rise to the possibility of introducing the usual methods used in the weak coupling open system in the polaron frame.

We studied the non-canonical equilibrium state of the SBM. The second-order perturbation theory in the po-

laron frame is used to obtain the equilibrium density matrix. The second-order results in the original frame are accurate only for weak SBC, whereas the full polaron results are accurate in the entire range of SBC for fast bath but only in the strong coupling regime for slow bath. The variational method is capable of interpolating between these two methods and is valid over a much broader range of parameters. Further, the non-canonical properties of the equilibrium states is revealed and the eigenbasis in the polaron frame are considered as the preferred basis for decoherence.

We then applied the polaron transformed Redfield equation to solve the steady states of non-equilibrium open systems. (i) In a one-dimensional disordered chain, the diffusion coefficient is shown to be linearly proportional to the exciton-phonon coupling strength in the weak coupling limit, while in the strong coupling limit, the diffusion coefficient depends on the phonon bath relaxation time which is the character of the hopping transport behavior. (ii) The heat transfer through a two-level quantum dot which connects with two separate baths was also investigated. The non-monotonic energy flux and differential thermal conductance were calculated following a similar polaron approach. (iii) When the three-level system is connected with three different heat baths, a heat engine model is thus constructed to study the steady state energy transfer flux and energy conversion efficiency. The steady state coherence and population inversion affect the efficiency obviously. In both the weak and strong coupling limits, the PTRE is coincidence with the Redfield equation and the Fermi's golden rule, which further verifies the validity of the polaron approach.

Acknowledgements D. Xu and J. Cao acknowledge the National Science Foundation (NSF) of the US (Grant No. CHE-1112825).

Appendix A Correlation functions in Eq. (18)

The non-vanishing bath correlation functions in Eq. (18) are

$$C_{xx}(\tau)=\frac{\Delta_\kappa^2}{8}\left(\mathrm{e}^{\phi(\tau)}+\mathrm{e}^{-\phi(\tau)}-2\right), \tag{A1}$$

$$C_{yy}(\tau)=\frac{\Delta_\kappa^2}{8}\left(\mathrm{e}^{\phi(\tau)}-\mathrm{e}^{-\phi(\tau)}\right), \tag{A2}$$

$$C_{zz}(\tau)=\int_0^\infty\frac{\mathrm{d}\omega}{\pi}J(\omega)[1-F(\omega)]^2\frac{\cosh((\beta-2\tau)\omega/2)}{\sinh(\beta\omega/2)}, \tag{A3}$$

$$C_{zy}(\tau)=-C_{yz}(\tau)$$

$$=\mathrm{i}\Delta_\kappa\int_0^\infty\frac{\mathrm{d}\omega}{\pi}\frac{J(\omega)}{\omega}F(\omega)[1-F(\omega)]\cdot\frac{\sinh((\beta-2\tau)\omega/2)}{\sinh(\beta\omega/2)}, \tag{A4}$$

where

$$\phi(\tau)=4\int_0^\infty\frac{\mathrm{d}\omega}{\pi}\frac{J(\omega)}{\omega^2}F(\omega)^2\frac{\cosh((\beta-2\tau)\omega/2)}{\sinh(\beta\omega/2)}. \tag{A5}$$

The correlation functions in the off-diagonal parts of the RDM are given by

$$S_x(\tau)=\frac{\Delta_\kappa^2}{2\Lambda^2}+\frac{\epsilon\,\mathrm{sech}(\beta\Lambda/2)}{2\Lambda^2}\{\epsilon\cosh[\frac{\Lambda}{2}(\beta-2\tau)]+\Lambda\sinh[\frac{\Lambda}{2}(\beta-2\tau)]\}, \tag{A6}$$

$$S_y(\tau)=-\frac{\mathrm{i}}{2}\mathrm{sech}(\beta\Lambda/2)\{\cosh[\frac{\Lambda}{2}(\beta-2\tau)]+\frac{\epsilon}{\Lambda}\sinh[\frac{\Lambda}{2}(\beta-2\tau)]\}. \tag{A7}$$

The bath correlation functions are $K_x(\tau)=2C_x(\tau)/\Delta$ and $K_y(\tau)=2\mathrm{i}C_y(\tau)/\Delta$. Note that the first-order correction here is again linked with the above-defined bath correlation function $C_{nn}(\tau)$. So, by construction, our perturbation theory for off-diagonal elements of RDM works even better for stronger SBC coupling.

Appendix B Redfield tensor in Eqs. (42) and (43)

The Redfield tensor in Eqs. (42) and (43) are given as

$$R_{\mu\nu,\mu'\nu'}=\Gamma_{\nu'\nu,\mu\mu'}+\Gamma^*_{\mu'\mu,\nu\nu'}-\delta_{\nu\nu'}\sum_\kappa\Gamma_{\mu\kappa,\kappa\mu'}-\delta_{\mu\mu'}\sum_\kappa\Gamma^*_{\nu\kappa,\kappa\nu'}, \tag{B1}$$

$$\Gamma_{\mu\nu,\mu'\nu'}=\sum_{mnm'n'}J_{mn}J_{m'n'}\langle\mu|m\rangle\langle n|\nu\rangle\langle\mu'|m'\rangle\langle n'|\nu'\rangle\times K_{mn,m'n'}(\omega_{\nu'\mu'}), \tag{B2}$$

where $K_{mn,m'n'}(\omega)$ is the half-Fourier transform of the bath correlation function

$$K_{mn,m'n'}(\omega)=\int_0^\infty\mathrm{e}^{\mathrm{i}\omega t}\langle V_{mn}(t)V_{m'n'}(0)\rangle_{\tilde{H}_B}\,\mathrm{d}t. \tag{B3}$$

Appendix C Details in non-equilibrium energy flux of Eq. (48)

The relaxation rate in Eq. (48) can be rewritten as

$$\phi_{e(o)}(\omega) = (2\pi)^{-1} \int_{-\infty}^{\infty} \mathrm{d}\omega' C_{e(o)}(\omega, \omega'). \tag{C1}$$

The corresponding kernel functions are given by

$$C_e(\omega, \omega') = \frac{1}{2} \sum_{\sigma=\pm} C_L^{\sigma}(\omega - \omega') C_R^{\sigma}(\omega') - \delta(\omega'), \tag{C2}$$

$$C_o(\omega, \omega') = \frac{1}{2} \sum_{\sigma=\pm} \sigma C_L^{\sigma}(\omega - \omega') C_R^{\sigma}(\omega'), \tag{C3}$$

where

$$C_v^{\pm}(\omega') = \int_{-\infty}^{\infty} \mathrm{d}\tau \mathrm{e}^{\mathrm{i}\omega'\tau \pm Q_v(\tau)} \tag{C4}$$

describes the rate density of the vth bath absorbing (emitting) energy $\omega(-\omega)$, obeying the detailed balance relation as $C_v^{\pm}(\omega')/C_v^{\pm}(-\omega') = \mathrm{e}^{\beta_v \omega'}$. And

$$Q_v(\tau) = \int_0^{\infty} \mathrm{d}\omega \frac{J_\nu(\omega)}{\pi\omega^2} [\cos(\omega\tau) \coth(\beta_\nu \omega/2) - \mathrm{i}\sin(\omega\tau)]. \tag{C5}$$

References

1. A. G. Redfield, The theory of relaxation processes, *Adv. Magn. Reson.* 1, 1 (1965)
2. G. Lindblad, On the generators of quantum dynamical semigroups, *Commun. Math. Phys.* 48(2), 119 (1976)
3. H. P. Breuer and F. Petruccione, The Theory of Open Quantum Systems, New York: Oxford University Press, 2002
4. J. Cao, A phase-space study of Bloch–Redfield theory, *J. Chem. Phys.* 107(8), 3204 (1997)
5. S. A. Crooker, J. A. Hollingsworth, S. Tretiak, and V. I. Klimov, Spectrally resolved dynamics of energy transfer in quantum-dot assemblies: Towards engineered energy flows in artificial materials, *Phys. Rev. Lett.* 89(18), 186802 (2002)
6. D. Kim, S. Okahara, M. Nakayama, and Y. Shim, Experimental verification of Förster energy transfer between semiconductor quantum dots, *Phys. Rev. B* 78(15), 153301 (2008)
7. S. I. E. Vulto, M. A. de Baat, R. J. W. Louwe, H. P. Permentier, T. Neef, M. Miller, H. van Amerongen, and T. J. Aartsma, Exciton simulations of optical spectra of the FMO complex from the green sulfur bacterium *Chlorobium tepidum* at 6 K, *J. Phys. Chem. B* 102(47), 9577 (1998)
8. T. Brixner, J. Stenger, H. M. Vaswani, M. Cho, R. E. Blankenship, and G. R. Fleming, Two-dimensional spectroscopy of electronic couplings in photosynthesis, *Nature* 434(7033), 625 (2005)
9. G. S. Engel, T. R. Calhoun, E. L. Read, T. Ahn, T. Mancal, Y. C. Cheng, R. E. Blankenship, and G. R. Fleming, Evidence for wavelike energy transfer through quantum coherence in photosynthetic systems, *Nature* 446(7137), 782 (2007)
10. J. Wu, F. Liu, Y. Shen, J. Cao, and R. J. Silbey, Efficient energy transfer in light-harvesting systems (I): optimal temperature, reorganization energy and spatial–temporal correlations, *New J. Phys.* 12(10), 105012 (2010)
11. Y. Tanimura, Stochastic Liouville, Langevin, Fokker–Planck, and master equation approaches to quantum dissipative systems, *J. Phys. Soc. Jpn.* 75(8), 082001 (2006)
12. R. X. Xu and Y. J. Yan, Dynamics of quantum dissipation systems interacting with bosonic canonical bath: Hierarchical equations of motion approach, *Phys. Rev. E* 75(3), 031107 (2007)
13. N. Makri and D. E. Makarov, Tensor propagator for iterative quantum time evolution of reduced density matrices (I): Theory, *J. Chem. Phys.* 102(11), 4600 (1995)
14. J. Prior, A. W. Chin, S. F. Huelga, and M. B. Plenio, Efficient simulation of strong system-environment interactions, *Phys. Rev. Lett.* 105(5), 050404 (2010)
15. S. Tornow, R. Bulla, F. B. Anders, and A. Nitzan, Dissipative two-electron transfer: A numerical renormalization group study, *Phys. Rev. B* 78(3), 035434 (2008)
16. H. D. Meyer, U. Manthe, and L. Cederbaum, The multi-configurational time-dependent Hartree approach, *Chem. Phys. Lett.* 165(1), 73 (1990)
17. M. Thoss, H. Wang, and W. H. Miller, Self-consistent hybrid approach for complex systems: Application to the spin-boson model with Debye spectral density, *J. Chem. Phys.* 115(7), 2991 (2001)
18. M. Moix, Y. Zhao, and J. Cao, Equilibrium-reduced density matrix formulation: Influence of noise, disorder, and temperature on localization in excitonic systems, *Phys. Rev. B* 85(11), 115412 (2012)
19. J. Moix, J. Ma, and J. Cao, Förster resonance energy transfer, absorption and emission spectra in multichromophoric systems (III): Exact stochastic path integral evaluation, *J. Chem. Phys.* 142(9), 094108 (2015)
20. H. Fröhlich, Electrons in lattice fields, *Adv. Phys.* 3, 325 (1954)
21. T. Holstein, Studies of polaron motion, *Ann. Phys.* 8(3), 325 (1959)
22. R. Silbey and R. A. Harris, Variational calculation of the dynamics of a two level system interacting with a bath, *J. Chem. Phys.* 80(6), 2615 (1984)
23. R. A. Harris and R. Silbey, Variational calculation of the tunneling system interacting with a heat bath (II): Dynamics of an asymmetric tunneling system, *J. Chem. Phys.* 83(3), 1069 (1985)
24. M. Grover and R. Silbey, Exciton migration in molecular crystals, *J. Chem. Phys.* 54(11), 4843 (1971)
25. S. Jang, Y. C. Cheng, D. R. Reichman, and J. D. Eaves, Theory of coherent resonance energy transfer, *J. Chem. Phys.* 129(10), 101104 (2008)
26. A. Nazir, Correlation-dependent coherent to incoherent transitions in resonant energy transfer dynamics, *Phys. Rev. Lett.* 103(14), 146404 (2009)

27. D. P. S. McCutcheon and A. Nazir, Quantum dot Rabi rotations beyond the weak exciton–phonon coupling regime, *New J. Phys.* 12(11), 113042 (2010)
28. C. K. Lee, J. M. Moix, and J. Cao, Coherent quantum transport in disordered systems: A unified polaron treatment of hopping and band-like transport, *J. Chem. Phys.* 142(16), 164103 (2015)
29. C. K. Lee, J. Moix, and J. Cao, Accuracy of second order perturbation theory in the polaron and variational polaron frames, *J. Chem. Phys.* 136(20), 204120 (2012)
30. C. K. Lee, J. Cao, and J. Gong, Noncanonical statistics of a spin-boson model: Theory and exact Monte Carlo simulations, *Phys. Rev. E* 86(2), 021109 (2012)
31. H. Dong, S. Yang, X. F. Liu, and C. P. Sun, Quantum thermalization with couplings, *Phys. Rev. A* 76(4), 044104 (2007)
32. D. Z. Xu, S. W. Li, X. F. Liu, and C. P. Sun, Noncanonical statistics of a finite quantum system with non-negligible system-bath coupling, *Phys. Rev. E* 90(6), 062125 (2014)
33. C. Wang, J. Ren and J. Cao, Nonequilibrium energy transfer at nanoscale: A unified theory from weak to strong coupling, *Scientific Reports* 5, 11787 (2015)
34. D. Z. Xu, C. Wang, Y. Zhao, and J. Cao, Polaron effects on the performance of light-harvesting systems: A quantum heat engine perspective, *New J. Phys.* 18(2), 023003 (2016)
35. A. Ishizaki and G. R. Fleming, On the adequacy of the Redfield equation and related approaches to the study of quantum dynamics in electronic energy transfer, *J. Chem. Phys.* 130(23), 234110 (2009)
36. L. A. Pachón and P. Brumer, Computational methodologies and physical insights into electronic energy transfer in photosynthetic light-harvesting complexes, *J. Phys. Chem. Lett.* 2, 2728 (2011), arXiv: 1203.3978
37. H. J. Carmichael, Statistical Methods in Quantum Optics, Springer, 1999
38. A. J. Leggett, S. Chakravarty, A. T. Dorsey, M. P. A. Fisher, A. Garg, and W. Zwerger, Dynamics of the dissipative two-state system, *Rev. Mod. Phys.* 59(1), 1 (1987)
39. U. Weiss, Quantum Dissipative Systems, Singapore: World Scientific, 2008
40. J. Cao, Effects of bath relaxation on dissipative two-state dynamics, *J. Chem. Phys.* 112(15), 6719 (2000)
41. A. W. Chin, J. Prior, S. F. Huelga, and M. B. Plenio, Generalized polaron ansatz for the ground state of the sub-ohmic spin-boson model: An analytic theory of the localization transition, *Phys. Rev. Lett.* 107(16), 160601 (2011)
42. Q. J. Tong, J. H. An, H. G. Luo, and C. H. Oh, Quantum phase transition in the delocalized regime of the spin-boson model, *Phys. Rev. B* 84(17), 174301 (2011)
43. D. P. S. McCutcheon, N. S. Dattani, E. M. Gauger, B. W. Lovett, and A. Nazir, A general approach to quantum dynamics using a variational master equation: Application to phonon-damped Rabi rotations in quantum dots, *Phys. Rev. B* 84(8), 081305 (2011)
44. D. Ruelle, Statistical Mechanics: Rigorous Results, New York: Benjamin, 1969
45. R. P. Feynman, Statistical Mechanics. A set of lectures, Longman: Addison Wesley, 1998
46. M. D. Girardeau and R. M. Mazo, Advances in Chemical Physics, Vol. 24, New York: Wiley, 1973
47. R. Kubo, M. Toda, and N. Hashitsume, Statistical Physics (II): Nonequilibrium Statistical Mechanics, Berlin: Springer-Verlag, 1983
48. A. Nitzan, Chemical Dynamics in Condensed Phases: Relaxation, Transfer and Reactions in Condensed Molecular Systems, Oxford: Oxford University Press, 2006
49. R. P. Feynman and F. L. Jr Vernon, The theory of a general quantum system interacting with a linear dissipative system, *Ann. Phys.* 24, 118 (1963)
50. W. H. Zurek, Decoherence, einselection, and the quantum origins of the classical, *Rev. Mod. Phys.* 75(3), 715 (2003)
51. J. P. Paz and W. H. Zurek, Quantum limit of decoherence: Environment induced superselection of energy eigenstates, *Phys. Rev. Lett.* 82(26), 5181 (1999)
52. D. Braun, F. Haake, and W. T. Strunz, Universality of decoherence, *Phys. Rev. Lett.* 86(14), 2913 (2001)
53. W. G. Wang, J. B. Gong, G. Casati, and B. Li, Entanglement-induced decoherence and energy eigenstates, *Phys. Rev. A* 77(1), 012108 (2008)
54. C. Gogolin, Environment-induced super selection without pointer states, *Phys. Rev. E* 81(5), 051127 (2010)
55. E. N. Zimanyi and R. J. Silbey, Theoretical description of quantum effects in multi-chromophoric aggregates, *Philos. Trans. R. Soc. A* 370(1972), 3620 (2012)
56. A. Troisi and G. Orlandi, Charge-transport regime of crystalline organic semiconductors: Diffusion limited by thermal off-diagonal electronic disorder, *Phys. Rev. Lett.* 96(8), 086601 (2006)
57. T. Sakanoue and H. Sirringhaus, Band-like temperature dependence of mobility in a solution-processed organic semiconductor, *Nat. Mater.* 9(9), 736 (2010)
58. J. Singh, E. R. Bittner, D. Beljonne, and G. D. Scholes, Fluorescence depolarization in poly[2-methoxy-5-((2-ethylhexyl)oxy)-1,4-phenylenevinylene]: Sites versus eigenstates hopping, *J. Chem. Phys.* 131(19), 194905 (2009)
59. M. Bednarz, V. A. Malyshev, and J. Knoester, Temperature dependent fluorescence in disordered Frenkel chains: Interplay of equilibration and local band-edge level structure, *Phys. Rev. Lett.* 91(21), 217401 (2003)
60. J. Moix, J. Wu, P. Huo, D. Coker, and J. Cao, Efficient energy transfer in light-harvesting systems (III): The influence of the eighth bacteriochlorophyll on the dynamics and efficiency in FMO, *J. Phys. Chem. Lett.* 2(24), 3045 (2011)
61. G. T. de Laissardière, J. P. Julien, and D. Mayou, Quantum transport of slow charge carriers in quasicrystals and correlated systems, *Phys. Rev. Lett.* 97, 026601 (2006)

62. V. Coropceanu, J. Cornil, D. A. da Silva Filho, Y. Olivier, R. Silbey, and J. L. Bredas, Charge transport in organic semiconductors, *Chem. Rev.* 107(4), 926 (2007)
63. F. Ortmann, F. Bechstedt, and K. Hannewald, Theory of charge transport in organic crystals: Beyond Holstein's small-polaron model, *Phys. Rev. B* 79(23), 235206 (2009)
64. S. Ciuchi, S. Fratini, and D. Mayou, Transient localization in crystalline organic semiconductors, *Phys. Rev. B* 83(8), 081202 (2011)
65. Y. Cheng and R. J. Silbey, A unified theory for charge-carrier transport in organic crystals, *J. Chem. Phys.* 128(11), 114713 (2008)
66. J. M. Moix, M. Khasin, and J. Cao, Coherent quantum transport in disordered systems (I): The influence of dephasing on the transport properties and absorption spectra on one-dimensional systems, *New J. Phys.* 15(8), 085010 (2013)
67. C. Chuang, C. K. Lee, J. M. Moix, J. Knoester, and J. Cao, Quantum diffusion on molecular tubes: Universal scaling of the 1D to 2D transition, arXiv: 1511.01198 (2015)
68. A. O. Niskanen, Y. Nakamura, and J. P. Pekola, Information entropic superconducting microcooler, *Phys. Rev. B* 76(17), 174523 (2007)
69. K. Le Hur, Kondo resonance of a microwave photon, *Phys. Rev. B* 85(14), 140506 (2012)
70. M. Galperin, M. A. Ratner, and A. Nitzan, Molecular transport junctions: Vibrational effects, *J. Phys.: Condens. Matter* 19(10), 103201 (2007)
71. J. C. Cuevas and E. Scheer, Molecular Electronics: An Introduction to Theory and Experiment, Singapore: World Scientific, 2010
72. D. Segal and A. Nitzan, Spin-boson thermal rectifier, *Phys. Rev. Lett.* 94(3), 034301 (2005)
73. D. Segal, Stochastic pumping of heat: Approaching the Carnot efficiency, *Phys. Rev. Lett.* 101(26), 260601 (2008)
74. J. Ren, P. Hänggi, and B. Li, Berry-phase-induced heat pumping and its impact on the fluctuation theorem, *Phys. Rev. Lett.* 104(17), 170601 (2010)
75. A. Caldeira and A. J. Leggett, Influence of dissipation on quantum tunneling in macroscopic systems, *Phys. Rev. Lett.* 46(4), 211 (1981)
76. N. B. Li, J. Ren, L. Wang, G. Zhang, P. Hänggi, and B. Li, Phononics: Manipulating heat flow with electronic analogs and beyond, *Rev. Mod. Phys.* 84(3), 1045 (2012)
77. L. Zhu, S. Kirchner, Q. M. Si, and A. Georges, Quantum critical properties of the Bose–Fermi Kondo model in a large-Nlimit, *Phys. Rev. Lett.* 93(26), 267201 (2004)
78. K. Saito and T. Kato, Kondo signature in heat transfer via a local two-state system, *Phys. Rev. Lett.* 111(21), 214301 (2013)
79. A. Ishizaki and G. R. Fleming, Quantum coherence in photosynthetic light harvesting, *Annu. Rev. Condens. Matter Phys.* 3(1), 333 (2012)
80. J. L. Wu, R. J. Silbey, and J. Cao, Generic mechanism of optimal energy transfer efficiency: A scaling theory of the mean first-passage time in exciton systems, *Phys. Rev. Lett.* 110(20), 200402 (2013)
81. S. F. Huelga and M. B. Plenio, Vibrations, quanta and biology, *Contemp. Phys.* 54(4), 181 (2013)
82. M. Esposito, U. Harbola, and S. Mukamel, Nonequilibrium fluctuations, fluctuation theorems, and counting statistics in quantum systems, *Rev. Mod. Phys.* 81(4), 1665 (2009)
83. T. V. Tscherbul and P. Brumer, Long-lived quasistationary coherences in a V-type system driven by incoherent light, *Phys. Rev. Lett.* 113(11), 113601 (2014)
84. J. Olšina, A. G. Dijkstra, C. Wang, and J. Cao, Can natural sunlight induce coherent exciton dynamics? arXiv: 1408.5385 (2014)
85. H. T. Quan, Y. X. Liu, C. P. Sun, and F. Nori, Quantum thermodynamic cycles and quantum heat engines, *Phys. Rev. E* 76(3), 031105 (2007)
86. M. O. Scully, K. R. Chapin, K. E. Dorfman, M. B. Kim, and A. Svidzinsky, Quantum heat engine power can be increased by noise-induced coherence, *Proc. Natl. Acad. Sci. USA* 108(37), 15097 (2011)
87. K. E. Dorfman, D. V. Voronine, S. Mukamel, and M. O. Scully, Photosynthetic reaction center as a quantum heat engine, *Proc. Natl. Acad. Sci. USA* 110(8), 2746 (2013)
88. H. E. D. Scovil and E. O. Schulz-DuBois, Three-level masers as heat engines, *Phys. Rev. Lett.* 2(6), 262 (1959)
89. J. E. Geusic, E. O. Schulz-DuBios, and H. E. D. Scovil, Quantum equivalent of the carnot cycle, *Phys. Rev.* 156(2), 343 (1967)
90. E. Geva and R. Kosloff, The quantum heat engine and heat pump: An irreversible thermodynamic analysis of the three-level amplifier, *J. Chem. Phys.* 104(19), 7681 (1996)
91. E. Boukobza and D. J. Tannor, Three-level systems as amplifiers and attenuators: A thermodynamic analysis, *Phys. Rev. Lett.* 98(24), 240601 (2007)
92. D. Gelbwaser-Klimovsky and A. Aspuru-Guzik, Strongly coupled quantum heat machines, *J. Phys. Chem. Lett.* 6(17), 3477 (2015)
93. J. Cao and R. J. Silbey, Optimization of exciton trapping in energy transfer processes, *J. Phys. Chem. A* 113(50), 13825 (2009)
94. C. Wang, J. Ren, and J. Cao, Optimal tunneling enhances the quantum photovoltaic effect in double quantum dots, *New J. Phys.* 16(4), 045019 (2014)
95. A. G. Dijkstra, C. Wang, J. Cao, and G. R. Fleming, Coherent exciton dynamics in the presence of underdamped vibrations, *J. Phys. Chem. Lett.* 6(4), 627 (2015)